Check for updates

Earth and Space Science

RESEARCH ARTICLE
10.1029/2026EA005069

Geology and Chronology of the Lunar Taruntius Crater: Implications for the Retention Age of Lunar Ray Patterns and Lifetime of Lunar Explosive Volcanism

Longjiao Yu[1], Haijun Cao[1], Le Qiao[1], and Zongcheng Ling[1]

[1]Shandong Key Laboratory of Space Environment and Exploration Technology, Institute of Space Sciences, School of Space Science and Technology, Shandong University, Weihai, China

Key Points:

- The Taruntius crater formed prior to ~3.7 Ga
- Its ray system is controlled by compositional contrasts and exhibits complete optical maturity
- Only crater rays are insufficient as a diagnostic criterion for identifying Copernican-aged impact craters

Supporting Information:

Supporting Information may be found in the online version of this article.

Correspondence to:

H. Cao and L. Qiao,
Caohj@mail.sdu.edu.cn;
LeQiao@sdu.edu.cn

Citation:

Yu, L., Cao, H., Qiao, L., & Ling, Z. (2026). Geology and chronology of the lunar Taruntius crater: Implications for the retention age of lunar ray patterns and lifetime of lunar explosive volcanism. *Earth and Space Science*, *13*, e2026EA005069. https://doi.org/10.1029/2026EA005069

Received 30 JAN 2026
Accepted 1 JUN 2026

Author Contributions:

Funding acquisition: Haijun Cao, Le Qiao, Zongcheng Ling
Investigation: Haijun Cao
Methodology: Longjiao Yu
Project administration: Haijun Cao, Le Qiao, Zongcheng Ling
Software: Longjiao Yu
Validation: Longjiao Yu
Writing – original draft: Longjiao Yu

© 2026. The Author(s).
This is an open access article under the terms of the Creative Commons Attribution-NonCommercial-NoDerivs License, which permits use and distribution in any medium, provided the original work is properly cited, the use is non-commercial and no modifications or adaptations are made.

Abstract The Taruntius crater, situated between Maria Fecunditatis, Crisium, and Tranquillitatis, is characterized by a prominent bright ray system and a floor-fractured morphology and has long been interpreted as a relatively young Eratosthenian or Copernican crater. Here, we combine high-resolution imagery, topography, and multispectral data to characterize its morphology, composition, and chronology. Taruntius exhibits a complex internal structure, including central peaks, fractures, and ridges, and its regolith has reached full optical maturity. Elemental abundances of FeO (6.9–19.1 wt.%), TiO_2 (0–8.7 wt.%), and Th (3.0–3.4 ppm) indicate low-Ti and moderately Th-enriched compositions. Plagioclase dominates the crater rim and walls (>60 wt.%), whereas the central peaks and ejecta are characterized by reduced plagioclase (<45 wt.%) and enhanced pyroxene (>40 wt.%) with minor olivine (<10 wt.%). Basaltic materials identified within floor fractures record localized volcanic activity predating the impact event. Crater size-frequency distribution analysis yields a model age of 3.7 ± 0.03 Ga, placing the formation of Taruntius in the late Imbrian period. These results revise previous age estimates, demonstrate that prominent ray systems do not necessarily indicate young lunar craters, and highlight the importance of integrating compositional and chronological analyses in reconstructing lunar surface evolution.

Plain Language Summary Bright rays around the Taruntius crater were long thought to indicate that it formed relatively recently in lunar history. Using high-resolution images, elevation data, and spectral measurements, we re-examined the origin and age of this crater. We found basaltic rocks and volcanic ash deposits on the crater floor, showing that volcanic activity occurred there in the past. Our mineral and chemical analyses reveal that the bright rays are caused by differences in rock composition rather than by freshly exposed material, and that the surface has been altered by space weathering over long periods of time. By counting impact craters on the crater floor, we estimate an age of about 3.7 billion years, much older than previously believed. These results show that bright rays alone cannot be used to determine the age of lunar craters and provide new insights into the impact history and volcanic evolution of the Moon.

1. Introduction

Impact craters are among the most diagnostic landforms on the lunar surface. Due to the extremely low rates of surface weathering and erosion, together with widespread exposure of materials formed during different geological epochs (Wilhelms et al., 1987), the Moon preserves an exceptionally complete record of impact events throughout its history (Neukum et al., 2001). Lunar impact craters exhibit systematic variations in morphology with increasing diameter, reflecting changes in impact flux and target response, and are commonly classified into microcraters, simple craters, complex craters, and impact basins (Melosh, 1989).

Microcraters are small in diameter (usually at the millimeter or submillimeter scale) and typically display smooth-textured impact melt coatings on their rims and inner walls. Simple craters are bowl-shaped with raised rims and floors infilled by collapsed clastic materials (Hartung et al., 1975; Melosh, 1989). With increasing size, craters transition to complex forms, characterized by flattened floors, reduced depth-to-diameter ratios, terraced walls, and, in larger examples such as Copernicus (~93 km) and Tycho (~85 km), uplifted central peaks that may further evolve into peak rings (Hawke et al., 2004; Melosh, 1989). At the largest scale, impact basins such as the Orientale basin exhibit multiple concentric rings produced by large-scale collapse of the basin interior and display broad, gently sloping topography (Melosh, 1989; Wilhelms et al., 1987).

A striking feature associated with many young and well-preserved craters, including Copernicus, Tycho, and Lichtenberg, is the presence of bright, radially distributed crater rays (Hawke et al., 2004). These rays are generally interpreted as fine-grained impact ejecta emplaced radially outward from crater rims, extending to many crater diameters and commonly occurring as discontinuous deposits (Pieters et al., 1985). In the lunar geochronology, the Copernican period represents the youngest geological unit. Consequently, constraining the formation age of Copernicus crater is crucial to understanding the retention timescale of lunar crater rays (Hiesinger et al., 2012).

Early constraints on the age of Copernicus crater were obtained through isotopic dating of KREEP glass samples returned by the Apollo 12 mission (Meyer et al., 1971). Subsequent works employing different isotopic systems yielded ages consistently younger than ~900 Ma (Eberhardt et al., 1973; Wentworth et al., 1994). Using remote sensing data, Hawke et al. (2004) examined the optical maturity and compositional characteristics of ejecta blankets at Copernicus, Tycho, and Lichtenberg, and proposed three mechanisms capable of producing crater rays: (a) compositional contrasts, such as bright highland materials superposed on darker mare units; (b) differences in optical maturity between freshly excavated and surrounding regolith; and (c) combined effects of both processes. Notably, the rays of Lichtenberg crater were shown to be dominated by compositional contrasts. Crater size-frequency distribution (CSFD) analyses indicate that Lichtenberg formed earlier than 1.68 Ga (Hiesinger et al., 2003), implying that crater rays may persist substantially longer than the timescale required for surface materials to reach optical maturity.

Taruntius crater is a complex impact structure characterized by bright rays (Figure 1). Clementine data reveal the presence of pyroclastic deposits within the crater, indicating past episodes of volcanic activity (Gaddis et al., 2003). Early geological mapping assigned Taruntius crater to the Copernican period (Wilhelms & McCauley, 1971). However, subsequent studies showed that its ray system primarily reflects compositional contrasts rather than optical immaturity, prompting its reclassification to the Eratosthenian system (Hawke et al., 2004). Although some uncertainty remains regarding its model age, Taruntius is generally considered relatively young. Thus, constraining its model age may provide important insights into the timing of the cessation of lunar explosive volcanic activities.

Here, we focus on the formation age and geological evolution of the Taruntius crater. We analyze its topographic and geomorphic characteristics using high-resolution lunar imagery and determine the absolute model age of the crater floor through crater size-frequency distribution measurements. To further clarify the origin of the Taruntius ray system and constrain the persistence of lunar crater rays, we examine the elemental, mineralogical, and optical maturity characteristics of the Taruntius region using multispectral and hyperspectral remote sensing data.

2. Geologic Setting of Taruntius Crater

Taruntius crater (46.2°E, 5.1°N) is a representative floor-fractured crater (FFC) on the lunar nearside (Figure 1). FFCs are a unique class of impact structures characterized by anomalously shallow floors and extensive fracture networks, commonly interpreted as the surface expression of magmatic intrusion or volcanic modification beneath crater floors (Jozwiak et al., 2012, 2015, 2017, 2018; Schultz, 1976).

Regionally, Taruntius occupies a transitional position among several major nearside lunar maria, including Mare Tranquillitatis to the northwest, Mare Crisium to the northeast, and Mare Fecunditatis to the south (Figure 1a). This setting reflects the combined influence of multiple impact basin formation events and subsequent mare volcanism.

Mare Tranquillitatis, northwest of Taruntius, is one of the oldest and most prominent nearside maria, hosting basalts with eruption ages of ~3.6–3.8 Ga (Hiesinger et al., 2000). These basalts are FeO- and TiO_2-rich and associated with abundant volcanic constructs, including numerous domes (Qiao et al., 2021). Unlike other major neighboring mare regions such as Serenitatis, Crisium, and Fecunditatis, Mare Tranquillitatis exhibits an irregular outer boundary, lacks well-defined multi-ring structures, and does not feature a pronounced central mascon (Neumann et al., 2015).

In the northeast of Taruntius, the Crisium basin is a large, well-preserved impact basin formed early in lunar history (Schultz, 1996). Extensive basaltic volcanism subsequently flooded the basin floor, producing a smooth, flat mare surface (Wilhelms & McCauley, 1971). Geological and geophysical data indicate the presence of mafic-rich impact melt sheets beneath the basalts (Bussey & Spudis, 2000). Crisium basin is bounded by extensive

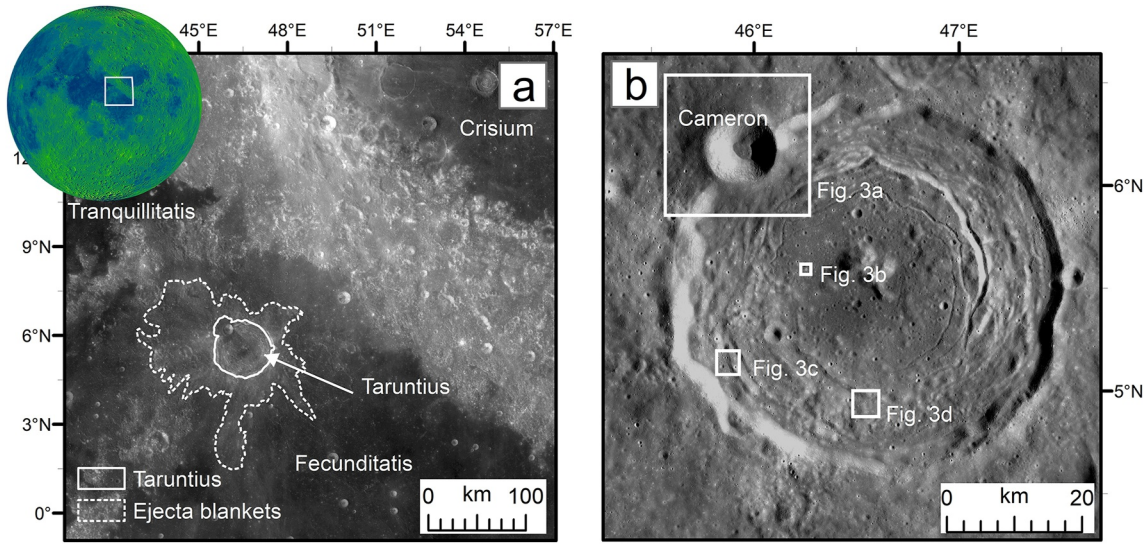


Figure 1. Geological context and morphology of the Taruntius crater. (a) Regional setting of Taruntius crater on the Chang'e-1 lunar base map (120 m/pixel). The white solid line outlines the crater rim, and the white dashed line indicates the ejecta blanket. Inset (upper left) shows the lunar nearside (LOLA WAC mosaic). (b) Detailed morphology of Taruntius crater from Kaguya TC mosaic (10 m/pixel). White boxes mark the locations of representative craters and the secondary crater systems shown in Figure 3. The projection is simple cylindrical projection.

highlands (Lu et al., 2021) and exhibits a circular morphology, a prominent mascon, concentric ridges, and numerous superposed impact craters (Byrne et al., 2015; Yu et al., 2024). In contrast to Tranquillitatis, its mare basalts overlie older highland materials, reflecting a complex interplay between impact basin formation and prolonged volcanic infilling (Runyon et al., 2020; Schultz & Spudis, 1983; Spudis & Sliz, 2017).

In the south of Taruntius, the Fecunditatis basin formed during the pre-Nectarian period (Thapa et al., 2025). Its mare fill is relatively thin and internally flat (Yue et al., 2025) and dominated by Ti-rich basalts that record multiple volcanic episodes (Thapa et al., 2025; Zhao et al., 2022). Like Tranquillitatis, Fecunditatis basin lacks a pronounced mascon (Zhao et al., 2022) and hosts diverse volcanic and tectonic landforms, including sinuous rilles, irregular mare patches, ring-moat domes, floor-fractured craters, and wrinkle ridges (Yue et al., 2025).

3. Data and Methodology

3.1. Data Sets

A suite of orbital data sets with complementary spatial resolutions and sensitivities was used to characterize the morphology, composition, and geological evolution of Taruntius crater and its surroundings.

To assess regional geomorphology and topography, we employed medium-resolution images from the LROC Wide Angle Camera (WAC; 100 m/pixel; Robinson et al., 2010) and merged topography derived from Kaguya/SELENE Terrain Camera (TC) and LRO Lunar Orbiter Laser Altimeter (LOLA) data (SLDEM 2015; 512 pixels/degree; vertical accuracy 3–4 m; Barker et al., 2016). Detailed topographic and morphological analyses were conducted using Kaguya TC images (10 m/pixel; Haruyama et al., 2008) and LROC Narrow Angle Camera (NAC) imagery (up to 0.6 m/pixel; Robinson et al., 2010), enabling characterization of crater features, slopes, and surface roughness within Taruntius and its vicinity. To assess subsurface structures, Bouguer gravity anomalies at a resolution of 16 pixels per degree (ppd) were analyzed using the GRGM1200A gravity field model (Goossens et al., 2020). Among the four available crustal thickness models (Wieczorek et al., 2013), Model 4 was adopted for the Taruntius crater region.

Spectroscopic data sets from Kaguya Multi-band Imager (MI; 20 m/pixel) and the Moon Mineralogy Mapper (M^3; Pieters et al., 2009) were employed to constrain the composition of pyroclastic deposits within the crater. Using established algorithms (Lemelin et al., 2015; Otake et al., 2012), we derived Fe and Ti abundances from MI data, with estimated uncertainties of ~1 wt.% for FeO and ~0.43 wt.% for TiO_2. Th content was

obtained from the Lunar Prospector Gamma-Ray Spectrometer (LP GRS; Lawrence et al., 2002), and Mg# map distributions were obtained from MI data (Zhang et al., 2023). Quantitative mineralogical analysis of major rock-forming minerals, including olivine, clinopyroxene, orthopyroxene, and plagioclase, was obtained using global mineral abundance maps (60 m/pixel) derived from Kaguya MI data and radiative transfer modeling (Lemelin et al., 2019).

Surface maturity was assessed from MI data following the methods of Lemelin et al. (2015) and Lucey et al. (2000), and rock abundance maps were generated at 128 pixel/degree (ppd) resolution (Bandfield et al., 2011). Thermal properties of the regolith were evaluated using H-parameter maps from Diviner data (128 ppd; Elder et al., 2017). Finally, the crater rays of Taruntius crater were mapped using Chang'e-1 data (120 m/pixel; Li et al., 2010). The flat inner crater region was subdivided into geological units based on Kaguya TC imagery and the map of TiO_2 derived from Kaguya MI data, and the crater age was estimated using CSFD analysis following Neukum et al. (2001).

3.2. Chemical Composition

Otake et al. (2012) developed an algorithm to estimate titanium content from Kaguya MI reflectance data, defined as:

$$\theta_{Ti} = \arctan\left[\frac{\frac{R_{415}}{R_{750}} - 0.208}{R_{750} - (-0.108)}\right]$$

$$\mathrm{TiO_2\ (wt.\%)} = 0.72 \times \theta_{\mathrm{Ti}}^{14.964}$$

Here, R_{415} and R_{750} correspond to MI reflectance at 415 and 750 nm (channels 1 and 2), respectively. θ_{Ti} is spectral angular parameters, and TiO_2 is the derived mass fractions on the lunar surface.

Lemelin et al. (2015) recalibrated algorithms of FeO. The refined method for estimating FeO content from MI reflectance is expressed as:

$$\theta_{\mathrm{Fe1}} = -\arctan\left[\frac{\frac{R_{950}}{R_{750}} - 1.39}{R_{750} - 0.04}\right]$$

$$\theta_{\mathrm{Fe2}} = 0.0656\mathrm{e}^{(3.6681 \times \theta_{\mathrm{Fe1}})}$$

$$\mathrm{FeO\ (wt.\%)} = 1.0708 \times \theta_{\mathrm{Fe2}} - 0.3986$$

Here, R_{750} and R_{950} correspond to MI reflectance at 750 and 950 nm (channels 2 and 4), respectively.

3.3. Optical Maturity

Optical maturity (OMAT) is a widely used index for assessing the maturity of lunar soils (Hou et al., 2022). For Kaguya MI data, OMAT is calculated following Lemelin et al. (2019) and Lucey et al. (2000) as:

$$R_{750\mathrm{corr}} = R_{750} * 1.51 + 0.020$$
$$R_{950\mathrm{corr}} = R_{950} * 1.38 + 0.022$$
$$\mathrm{O_{OMAT}} = \left[(R_{750\mathrm{corr}} - x_0) - \left(\frac{R_{950\mathrm{corr}}}{R_{750\mathrm{corr}}} - y_0\right)^2\right]^{1/2}$$

Here, R_{750} and R_{950} are the reflectances of MI data at 750 and 950 nm, respectively. The parameters x_0 and y_0 represent the reference reflectivity and ratio values. For Clementine multispectral data, these are 0.08 and 1.19, respectively (Lucey et al., 2000).

3.4. Age Determination From CSFDs

CSFD analysis provides a method for estimating surface ages based on cumulative crater populations (Hiesinger et al., 2000). On geologically homogeneous units, surfaces that predate crater saturation exhibit higher cumulative densities of primary craters within a given size range. By fitting the observed CSFDs to a crater production function (PF), the cumulative crater density $N(D)$ for craters with diameters ≥1 km can be determined. Crater Tools in ArcGIS was used to delineate various geological units for dating and extract impact craters, and CSFD fitting and spatial analysis was performed using the CraterStats software (Kneissl et al., 2011; Michael et al., 2012; Michael & Neukum, 2010).

Following Neukum et al. (2001), the crater production function is:

$$\log_{10} N(D) = a_0 + \sum_{n=1}^{11} a_n (\log_{10} D)^n \ (10\text{m} < D < 300\text{km})$$

where $N(D)$ (km^{-2}) denotes the cumulative density of impact craters larger than D (km).

Surface ages are derived using the chronological function (CF) of Neukum et al. (2001):

$$N(1) = 5.44 \times 10^{-14} \left(e^{6.93T} - 1\right) + 8.38 \times 10^{-4} T$$

where T is the absolute model age (AMA) in billion years (Ga).

4. Results

4.1. Geomorphology

Taruntius crater exhibits the characteristic morphology of a complex impact structure, with a diameter of 58 km and a maximum rim-to-floor elevation difference of ~1,100 m, resulting in a relatively low depth-to-diameter ratio of 0.017. Topographic analysis reveals a southwest-high, northeast-low gradient, with an elevation difference of ~600 m across 60 km (Figures 1b, 2a and 2b). The lunar crustal thickness in the region shows a gradual thinning from southwest to northeast, ranging from 25 to 33 km (Figure 2e). No local significant mass concentrations are observed (Figure 2f). Previous work suggests that shallower depth of the crater primarily reflects floor uplift rather than rim degradation or infilling (Wichman & Schultz, 1996).

The crater exhibits pronounced zonal variations in surface morphology (Figure 1b). The rim is dominated by plagioclase-rich highland ejecta, while the floor displays densely distributed secondary features, including irregular kipukas, concentric arc-shaped ridges, and tectonically induced floor fractures (Figures 1b, 2b and 3). Stress-release landforms, such as marginal depressions, are also present (Figure 2b). Roughness analysis shows the highest variability along the central peak, crater rim, and adjacent walls (Figure 2d), likely resulting from slope-driven wall material sliding.

The central plain, covering ~440 km^2, is dominated by low-albedo, flat mare basaltic units with slopes <4° (Figures 2c and 2d). Unlike young impact craters such as Aristarchus and Tycho, the floor of Taruntius crater lacks typical, large-scale impact melt flow morphologies (Lev et al., 2021; Mustard et al., 2011), indicative of late-stage volcanic infill. Crater dynamics modeling suggests that the Taruntius impact reached the theoretical peak transient cavity depth, producing intense target fragmentation and viscoelastic rebound (Melosh, 1979). This high-energy environment facilitated rapid central peak uplift (Figure 1b) and the formation of dense shock-fractured vein networks in the crater floor, providing key structural constraints on complex crater formation mechanisms.

4.2. Impact Craters

Impact craters within Taruntius crater exhibit pronounced topographic variability (Figure 3), ranging from fresh craters to heavily degraded structures. These fresh craters usually featured sharply defined edges and preserved ejecta blankets (Figures 3a and 3b). The largest recently formed crater, located in the northwestern rim crest, is a dark halo crater and measures ~10 km in diameter and ~2.2 km in depth. In contrast, degraded crater walls display gentle slopes of ~5° and surfaces with a characteristic "elephant-hide" texture, indicative of modification by regolith-driven downhill creep.

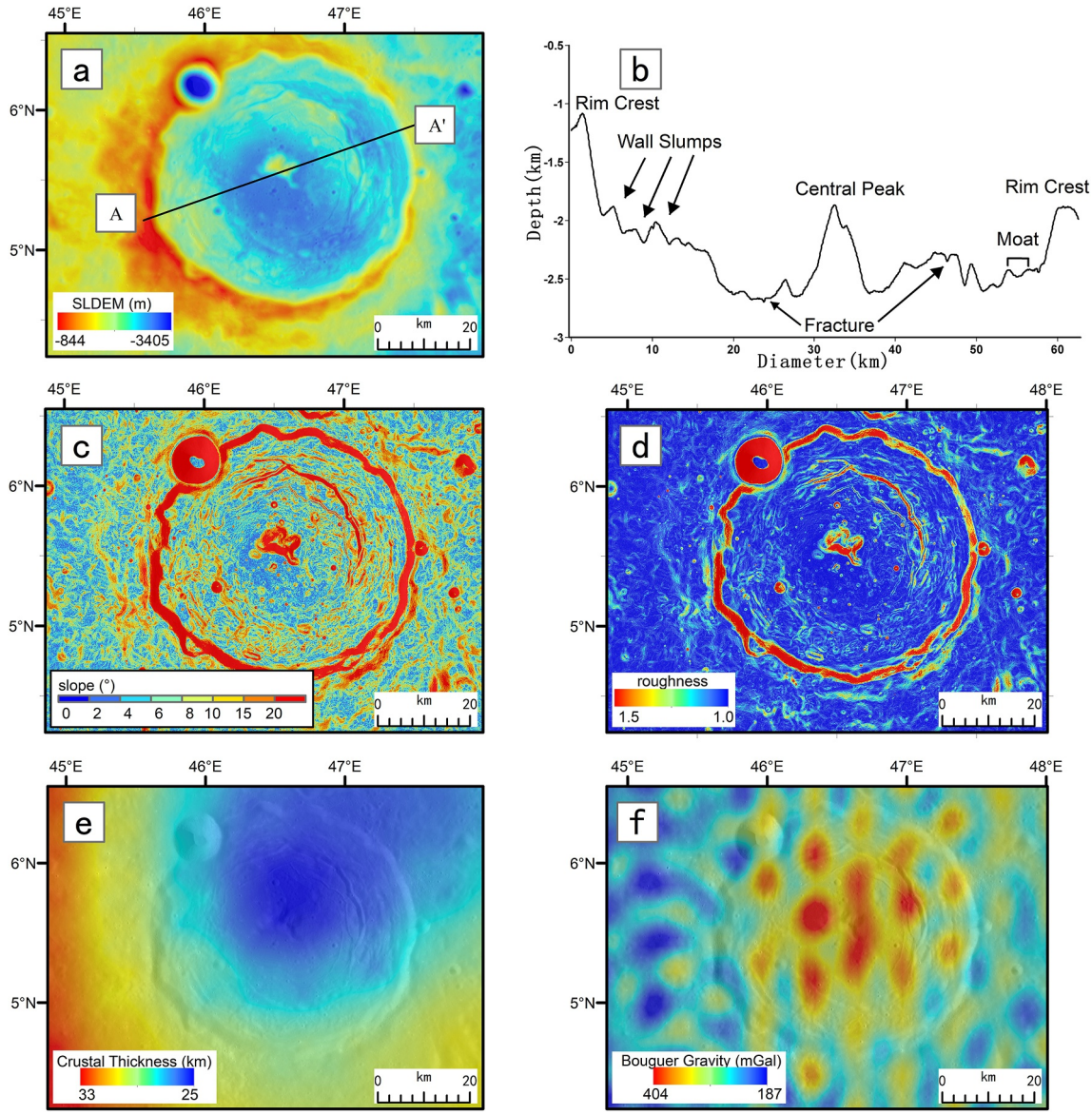


Figure 2. Topographic, slope, roughness, crustal thickness, and gravity characteristics of the Taruntius region. (a) SLDEM2015 topography (merged Kaguya/SELENE-TC and LRO/LOLA DEM) overlaid on a WAC mosaic. (b) Elevation profile along the A–A′ section showing depth variations. (c) Slope map derived from SLDEM2015 overlaid on WAC imagery. (d) Surface roughness map derived from SLDEM2015 overlaid on WAC imagery. (e) Lunar crustal thickness distribution overlaid on WAC imagery. (f) Bouguer gravity anomaly map overlaid on WAC imagery. The projection is simple cylindrical projection.

Secondary crater chains are observed as clustered, chain-like depressions with diameters <500 m (Figures 3c and 3d), lacking evidence of boulder accumulation. These features likely formed from the ballistic emplacement of clastic material ejected during the formation of larger impact craters (e.g., the Cameron crater), consistent with models of secondary cratering on the lunar surface.

4.3. Mineralogy and Chemical Compositions

4.3.1. Chemical Compositions

TiO_2 and FeO abundance maps derived from Kaguya MI data reveal marked elemental heterogeneity across Taruntius crater and its surrounding radial patterns (Figures 4a and 4b). TiO_2 concentrations range up to 8.7 wt.% with a mean of 3.7 wt.%, whereas FeO varies between 6.9 and 19.0 wt.% with an average of 14.2 wt.%. Within the crater and its ejecta blanket, the central peak and adjacent zones exhibit relatively elevated TiO_2 values (up to

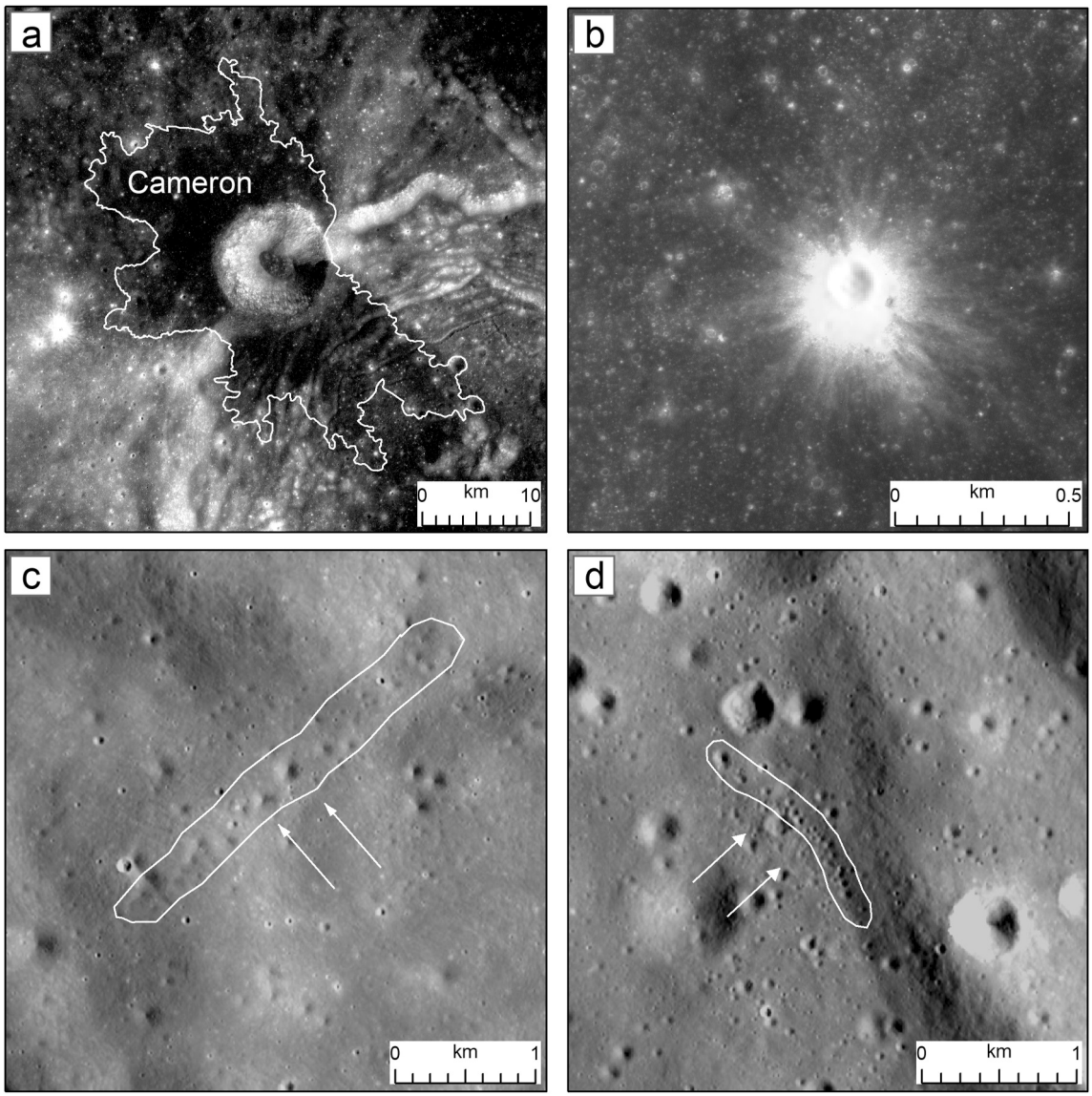


Figure 3. Impact craters and crater clusters in the Taruntius region. (a) The regionally largest impact crater (~10 km diameter) at the northwest rim crest of Taruntius. (b) One of the freshest small craters (~140 m diameter) with bright rays, LROC NAC image. (c, d) Secondary crater chains and clusters.

6 wt.%), whereas regions near crater walls and rims display consistently low titanium (<3.0 wt.%), with minimal local variation. Beyond the ejecta blanket, elevated titanium may reflect the presence of basaltic lithologies (Figures 4a and 5).

Iron distribution is strongly heterogeneous. The central peak and adjacent zones are enriched in FeO (up to 18.5 wt.%), with a general decrease toward the crater rim. The decline varies directionally: the northwest direction shows a gradual decrease, whereas the southwest and southeast directions exhibit a steeper gradient. The areas outside the ejecta blanket maintain relatively high FeO, with notable enrichment to the south.

Th concentrations are moderately high (Figure 4c) and increase from southwest to northeast. Mg# abundances range from 41 to 75 (Figure 4d), with overall higher values in the crater floor and ejecta blanket, peaking near the rim. In contrast, the central peak and adjacent zones show relatively low Mg# values, reflecting petrological heterogeneity associated with magmatic differentiation or stratigraphic exposure. Collectively, these data indicate that the crater ejecta and ray deposits incorporate substantial highland ejecta material.

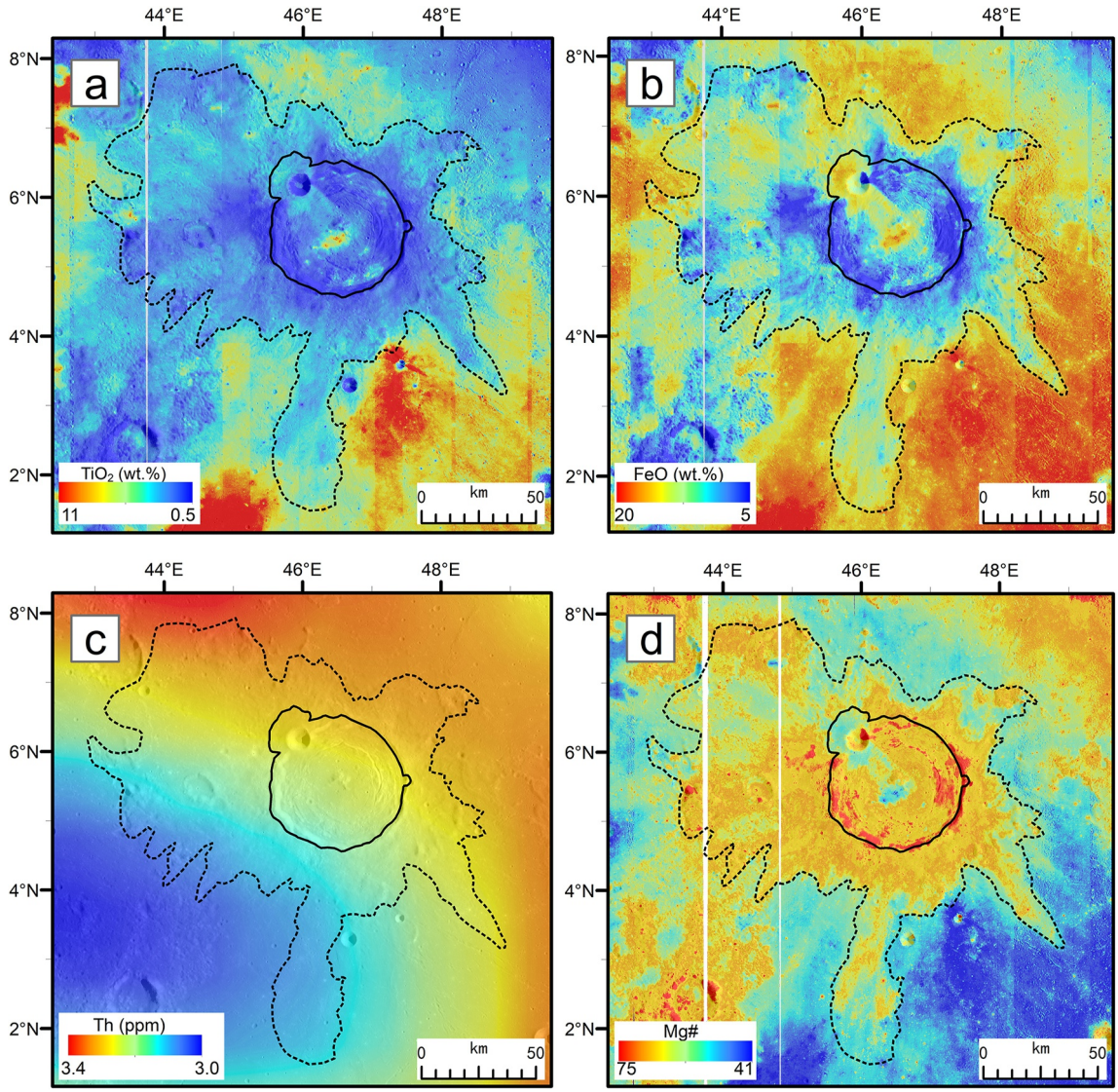


Figure 4. Elemental and compositional maps of the Taruntius region. (a) TiO_2 content, (b) FeO content, (c) Th content, and (d) Mg# distribution, each overlaid on the Kaguya TC image mosaic. The projection is simple cylindrical projection.

4.3.2. Mineralogy

Quantitative mineral abundance maps of major rock-forming phases derived from Kaguya MI data (Figure 5; Lemelin et al., 2019) show that the study area is dominated by plagioclase, with an average abundance of 50 wt.% ($1\sigma = 5$ wt.%), followed by clinopyroxene at 23 wt.% ($1\sigma = 4$ wt.%), orthopyroxene at 21 wt.% ($1\sigma = 4$ wt.%), and minor olivine at 7 wt.% ($1\sigma = 3$ wt.%).

Within the crater floor and its ejecta blanket, plagioclase is the predominant mineral phase, with pronounced enrichment along the crater walls and rim. Pyroxenes occur at moderate abundances, whereas olivine is consistently subordinate. Regions beyond the ejecta blanket are dominated by lunar mare basalts. Notably, the average plagioclase content near the Cameron crater and, together with the central peak of Taruntius, is ~46 wt.%, significantly lower than that of the surrounding units (~63 wt.%). In contrast, orthopyroxene, clinopyroxene, and olivine show marked enrichment in these areas, with abundance of 20, 26, and 9 wt.%, respectively.

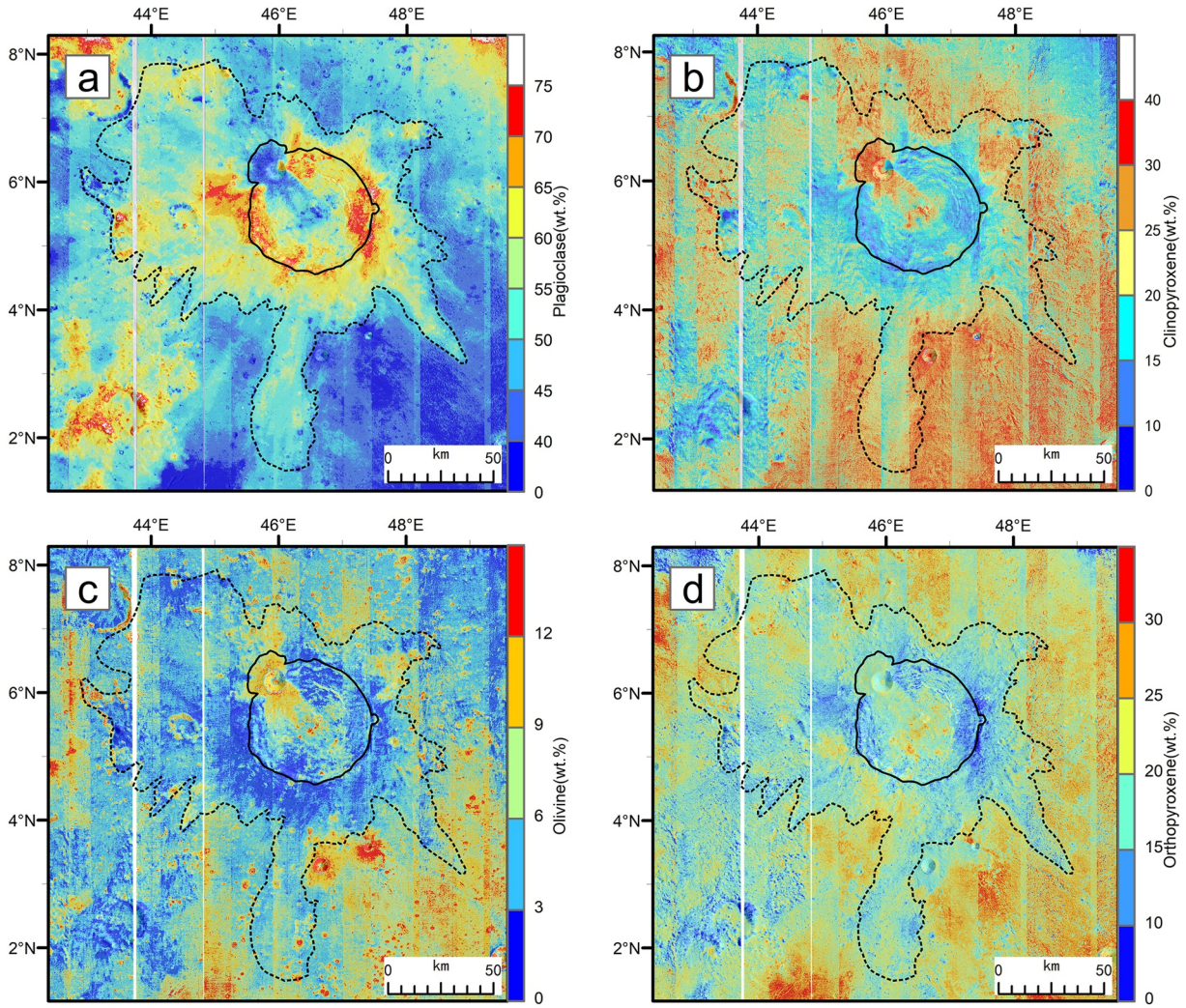


Figure 5. Kaguya MI-derived abundance maps of major rock-forming minerals, overlaid on the Kaguya TC image mosaic: (a) plagioclase, (b) clinopyroxene, (c) olivine, and (d) orthopyroxene. The projection is simple cylindrical projection.

4.3.3. Pyroclastic Deposits

MI 750 nm reflectance imagery and M^3 data (Figures 6s and 6b) reveal the presence of dark mantle deposits with reflectance values significantly lower than those of the surrounding terrains, concentrated near the central peak and partially along the floor-fracture zones of Taruntius crater. In the M^3 integrated band-depth color image (Figure 6d), these deposits appear as orange-toned units, consistent with the spectral characteristics of lunar pyroclastic materials (Besse et al., 2013).

False color composite images constructed using band ratios of red = R_{750}/R_{415}, green = R_{750}/R_{950}, and blue = R_{415}/R_{750} (Figure 6c) distinguish multiple compositional units with varying Ti–Fe contents across the Taruntius region, suggesting that volcanic activity occurred in more than one eruptive phase (Pieters et al., 1994). In these composites, red tones indicate relatively low Ti content, whereas blue tones correspond to higher Ti abundances (Wilhelms et al., 1987). Deposits exhibiting higher R750/R950 ratios display deeper 1 μm absorption bands and stronger mafic spectral signatures, whereas lower ratios correspond to shallower absorption features and weaker mafic characteristics (Gaddis et al., 2003). The spectral data further indicate enrichment of iron (>13 wt.%) in the area south to the central peak and within the mare regions beyond the ejecta blanket. Collectively, these dark mantle deposits constitute direct geological evidence for explosive volcanic activity within the Taruntius crater region (Head & Wilson, 1979).

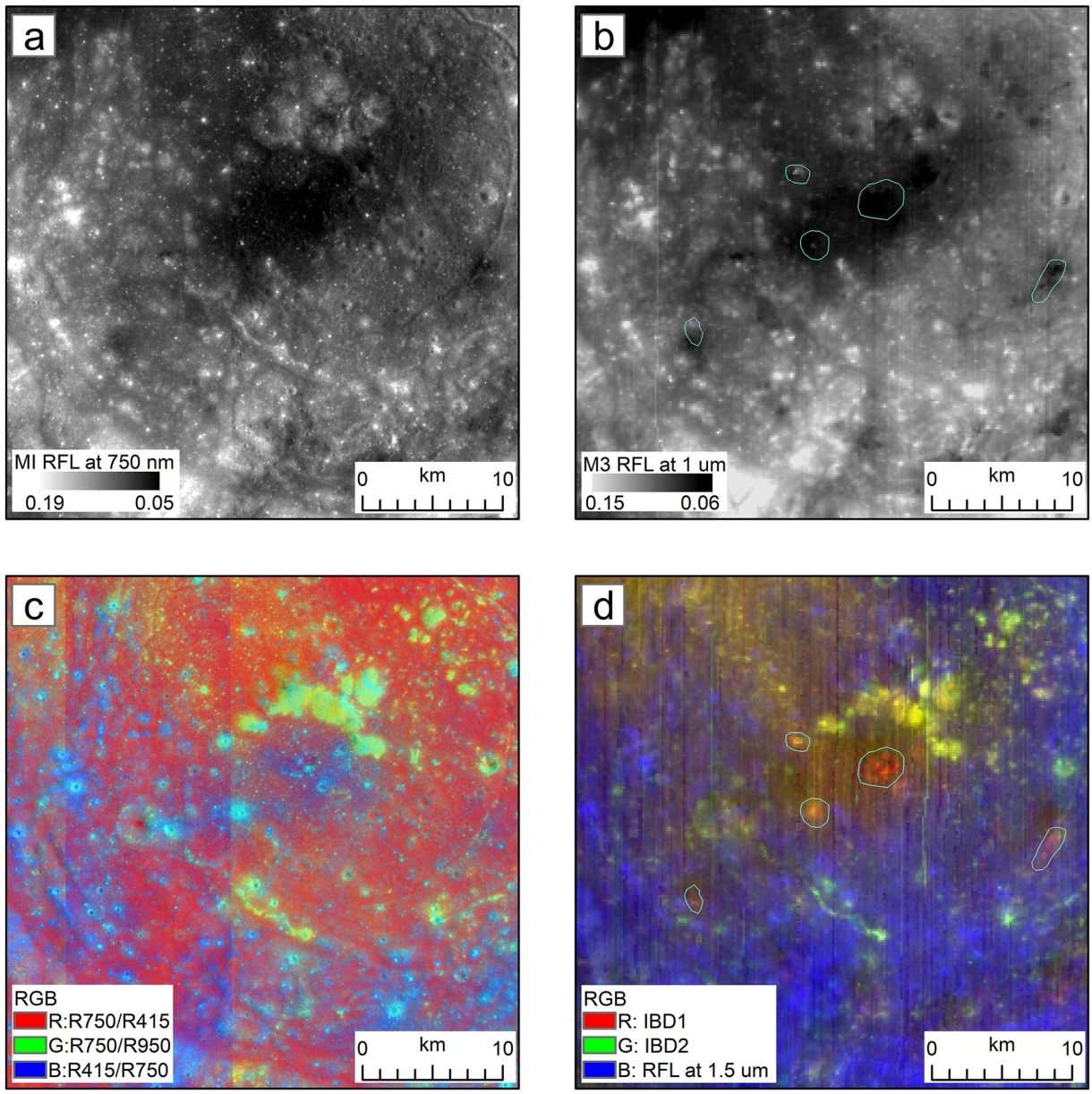


Figure 6. Pyroclastic deposits in Taruntius crater. (a, b) Reflectance maps showing pyroclastic deposits as dark areas: Kaguya MI at 750 nm (a) and M^3 at 1 μm (b). (c) Color composite from Kaguya MI (R: R_{750}/R_{415}, G: R_{750}/R_{950}, B: R_{415}/R_{950}) overlaid on Kaguya TC mosaic. (d) RGB composite from M^3 (R: integrated 1 μm band depth, G: integrated 2 μm band depth, B: reflectance at 1.5 μm) overlaid on Kaguya TC mosaic, with pyroclastic deposits appearing orange due to iron-bearing mineral signatures. The projection is simple cylindrical projection.

Mineralogical signatures within the fracture zones indicate the presence of a large amount of basaltic materials. The average abundances are ~47 wt.% plagioclase, ~45 wt.% pyroxene (including ~24 wt.% orthopyroxene and ~21 wt.% clinopyroxene), and ~8 wt.% olivine. Pyroclastic materials are predominantly distributed south to the central peak, whereas only limited occurrences are observed locally near the fracture zones. This composition pattern, combined with their spatial distribution, implies that most basaltic materials adjacent to the fracture zones (excluding pyroclastics regions) are more likely derived from the effusive volcanic regime during the late stage of volcanic activity after magma ascended to the lunar surface (Zhao et al., 2023). In addition, the dark halo crater (Cameron crater) surrounding the crater rim, together with its moderate iron content (~13 wt.%), suggests that the underlying mare surface is of volcanic origin.

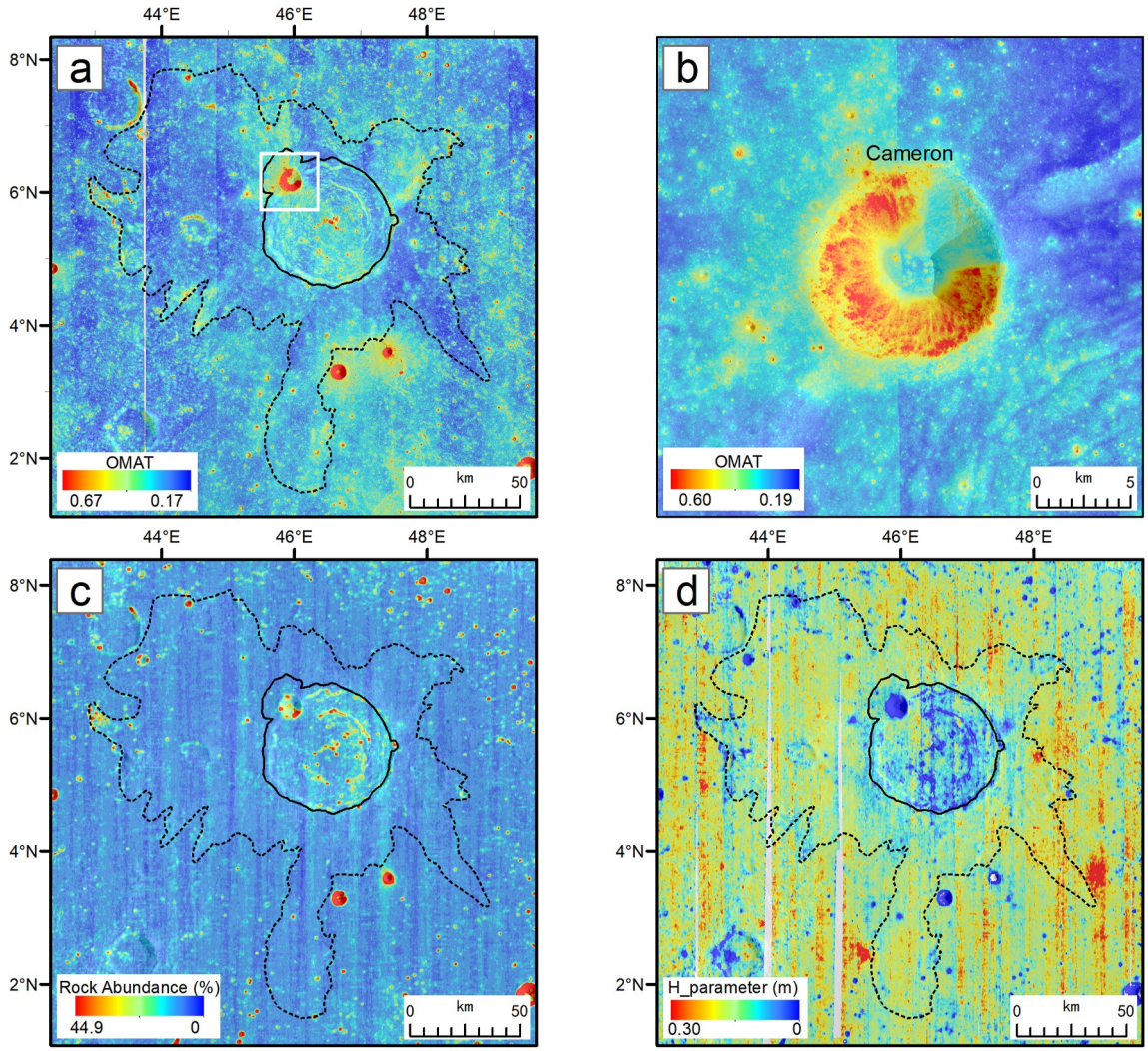


Figure 7. Space weathering and surface properties of the Taruntius region. (a, b) Optical maturity maps of (a) Taruntius and (b) Cameron craters, derived from Kaguya MI image, overlaid on the Kaguya TC image mosaic. Maps of rock abundance(c) and H-parameter (d), respectively, overlaid on the Kaguya TC mosaic. The projection is simple cylindrical projection.

4.4. Optical Maturity, Rock Abundance, and H-Parameter

Higher OMAT values correspond to optically immature surfaces that are generally younger in relative age (Hou et al., 2022). The calculated OMAT values for the study area range from 0.16 to 0.71, with a mean of 0.26 (Figure 7a). No pronounced contrast in optical maturity is observed between the ejecta blanket (averaging 0.26) and Mare Fecunditatis (averaging 0.25). In contrast, relatively high OMAT values characterize the young impact craters along the Cameron crater, the central peak, the circular fracture systems, and small fresh craters within the crater floor, indicating limited space-weathering modification. Overall, the ejecta blanket exhibits slightly lower OMAT values than the inner crater (averaging 0.28) and values comparable to those of the surrounding mature mare surfaces, suggesting that the ejecta materials have reached an advanced stage of optical maturation (Hawke et al., 2004).

Rock abundance (RA), defined as the fractional surface area occupied by rocks within a pixel, provides complementary constraints on the surface age and degradation state. It should be noted that clusters of small rocks may thermally mimic fewer larger rocks, potentially complicating interpretations of ejecta materials (Elder et al., 2017). The spatial distribution of RA (Figure 7c) shows a clear correspondence with OMAT, whereby regions of low rock abundance coincide with optically mature surfaces, and higher rock abundances are associated with higher OMAT values. The ejecta blanket of Taruntius does not display a significant enhancement in

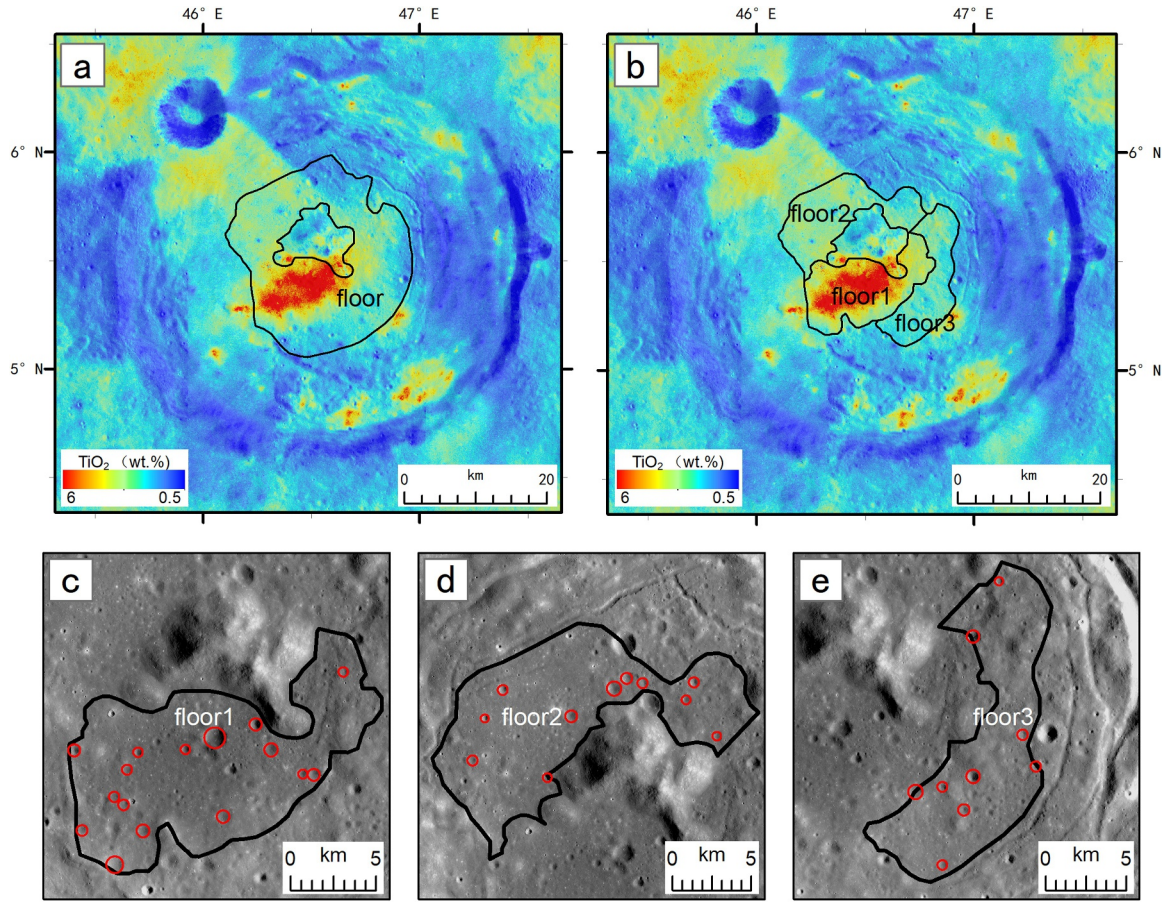


Figure 8. Crater count areas and results for surface age determination in Taruntius crater. (a) Relatively flat region on the crater floor, TiO_2 abundance image overlaid on the Kaguya TC mosaic. (b) Three independent geological units on the floor selected for crater counting. TiO_2 abundance image was overlaid on the Kaguya TC mosaic. (c–e) Crater count areas corresponding to floor1, floor2, and floor3 in (b), respectively, all three images are from the Kaguya TC morning map. The projection is simple cylindrical projection.

rock abundance relative to the surrounding terrains. In contrast, elevated RA values are observed at the Cameron crater, central peak, floor-fracture zone, and the clusters of small fresh craters within the Taruntius crater floor. Surface-exposed rocks on the Moon progressively degrade due to micrometeorite bombardment (Mendell, 1976), and younger craters therefore tend to preserve higher rock abundances. Previous studies have documented systematic decreases in rock abundance with increasing crater age (Ghent et al., 2014; Mendell, 1976). Accordingly, the relatively low RA values within the Taruntius ejecta blanket are consistent with an older formation age.

Thermal properties of the regolith were further assessed using the H parameter derived from Diviner nighttime temperature observations (Figure 7d). Lunar regolith typically exceeds 10 cm in thickness (Shkuratov & Bondarenko, 2001), and its bulk density increases exponentially with depth, a relationship parameterized by the H value (Vasavada et al., 2012). Because thermal inertia is approximately proportional to bulk density, lower H values indicate higher thermal inertia, which may reflect reduced porosity and/or enhanced abundances of subcentimeter rock fragments within the regolith (Elder et al., 2017). Within the Taruntius crater, several low-H units are identified. The ejecta blanket exhibits H values slightly higher than those of the crater floor but marginally lower than those of the surrounding terrains. We infer that these reduced H values likely result from the presence of fine-grained rock fragments mixed into the regolith, consistent with Apollo sample observations documenting abundant centimeter-scale clasts in lunar soils (Carrier et al., 1991).

The radially bright patterns surrounding Taruntius crater, which contrast with the darker adjacent mare surfaces, are interpreted to result from the emplacement of highland-derived materials during the impact event and subsequent modification. These materials possess distinct iron and titanium contents relative to the surrounding maria, producing the observed compositional and photometric contrasts (Hawke et al., 2004).

4.5. Chronology

4.5.1. Unit Divisions

The formation and subsequent modification of impact craters are controlled by multiple geological processes. Among the landforms produced during crater formation, continuous ejecta blankets and impact melt deposits are the most prominent and are therefore commonly selected for CSFD analyses aimed at constraining absolute crater ages (Melosh, 1989). Although impact melt ponds and ejecta blankets are theoretically emplaced contemporaneously, CSFD-derived ages of impact melt surfaces are often younger than those obtained from continuous ejecta blankets (Hiesinger et al., 2012). This discrepancy has been attributed to factors such as variations in locations or target properties and contamination by secondary craters (Shoemaker et al., 1968, 1969; Singer et al., 2020; Xie et al., 2019; Zanetti et al., 2017).

Accurate age determination using ejecta deposits additionally requires precise delineation of the ejecta extent (Neukum et al., 2001). Where ejecta thickness is insufficient to fully obscure pre-existing craters, crater populations formed both before and after the main impact may coexist on the ejecta surface, potentially biasing age estimates. In contrast, crater populations within crater floors are dominantly superposed after formation of the host crater, making these surfaces particularly suitable for CSFD analysis. Floor-based crater counts have been widely applied to constrain the ages of large lunar craters and to calibrate lunar chronology functions, including at Shackleton, Copernicus, and Tycho craters (Hiesinger et al., 2012).

Different geological units may record distinct geological events and evolutionary histories. Consequently, the CSFD method yields geologically consistent ages only when applied within a single, well-defined geological unit. Hiesinger et al. (2006) proposed a method for delineating geological units in lunar mare regions using multispectral images. Following the assumption that an individual geological unit is characterized by relatively homogeneous material properties, we identified multiple compositional units with distinct TiO_2 abundances on the floor of the Taruntius crater. To minimize the uncertainties associated with complex topography and heterogeneous surface textures, we selected three relatively flat impact melt units (slope $< 5°$) on the Taruntius crater floor (including floor1, floor2, and floor3) for crater dating (Figure 8). Areas characterized by steep slopes, prominent secondary crater chains, rough morphologies, or the central peak were excluded from the analysis. This targeted unit selection procedure improves the robustness of crater counts and enhances the reliability of the derived age constraints by focusing on surfaces with simplified geomorphology and optimal crater preservation.

4.5.2. The Formation Age of Taruntius Crater

CSFD measurements were performed using the production and chronology functions (Neukum et al., 2001). Based on spatial randomness analysis using Craterstats (Text S1 and Figures S1–S11 in Supporting Information S1; Kneissl et al., 2011; Michael & Neukum, 2010; Michael et al., 2012), craters with diameters ≥500 m were mapped for each selected floor unit, and the resulting age determinations are summarized in Table 1 and Figure 9.

Within floor1, 16 craters with diameters ≥500 m were identified over an area of 136 km^2, yielding a model age of 3.70 ± 0.06 Ga and an N(1) value of 1.20×10^{-2}. The corresponding CSFD curve closely follows the fitted isochron, indicating a statistically robust age estimate. Floor2 contains 11 craters ≥500 m in diameter across 127 km^2, resulting in a model age of 3.60 ± 0.09 Ga and an N(1) of 7.77×10^{-3}. Floor3 includes 9 craters ≥500 m in diameter within 97 km^2, corresponding to a model age of 3.70 ± 0.07 Ga and an N(1) of 1.07×10^{-2}. The combined floor area totals 441 km^2 and yields a comparable model age of 3.70 ± 0.03 Ga, with an N(1) value of 1.16×10^{-2}.

5. Discussions

5.1. Crater Ages and Their Uncertainties

The crater floor and continuous ejecta blanket of Taruntius crater formed contemporaneously during a single impact event. Accordingly, CSFD dating of different floor sub-units is expected to yield consistent model ages within statistical uncertainties. Our CSFD results are consistent with this expectation within the uncertainties of each subunit (Figure 9).

Among the individual units, floor2 yields the youngest model age and shows the poorest fit to the production function, whereas floor1 and floor3 exhibit slightly older ages. The combined floor unit produces an intermediate

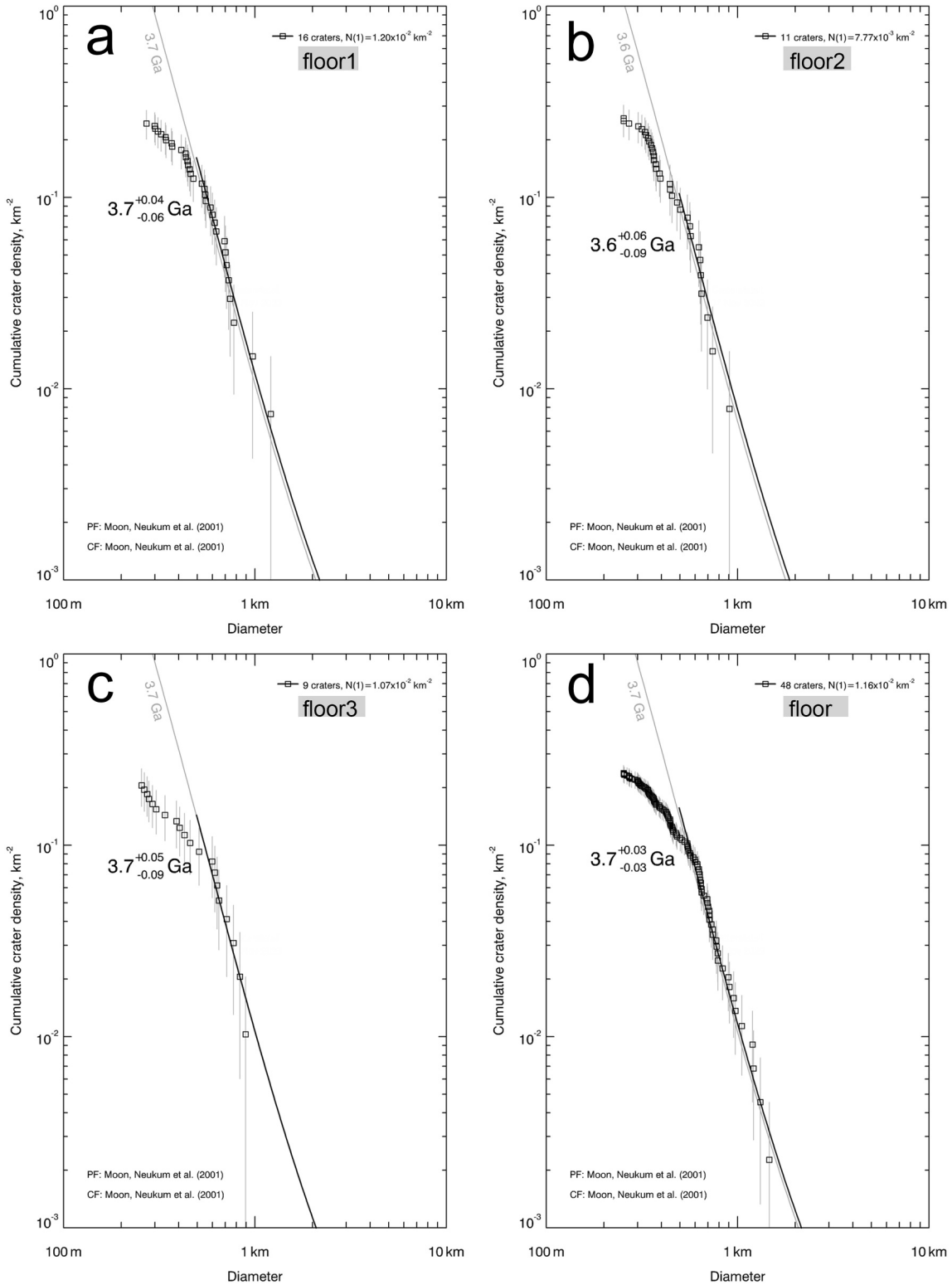


Figure 9. CSFD and surface age estimates for the Taruntius crater floor. (a–c) Regional CSFDs for floor1, floor2, and floor3, respectively. (d) Cumulative crater counts combining floor area. Only craters with diameters ≥500 m were used for fitting. Production and chronology functions (PF and CF) are from Neukum et al. (2001).

Table 1
Cumulative CSFDs and AMAs for Selected Regions of Taruntius Crater

Unit	Crater counting area(km^2)	Number of craters for age fitting	Crater diameter for age fitting (km)	N(1) (km^{-2})	AMA
floor1	136	16	>0.5	$1.20 * 10^{-2}$	$3.7^{+0.04}_{-0.06}$ Ga
floor2	127	11	>0.5	$7.77 * 10^{-3}$	$3.6^{+0.06}_{-0.09}$ Ga
floor3	97	9	>0.5	$1.07 * 10^{-2}$	$3.7^{+0.05}_{-0.07}$ Ga
floor	441	51	>0.5	$1.16 * 10^{-2}$	$3.7^{+0.03}_{-0.03}$ Ga

model age that falls within the range defined by the three individual sub-units. The formation of the Cameron crater on the northwestern rim of Taruntius likely emplaced ejecta onto the Taruntius crater floor, partially mantling pre-existing craters within the floor2 area and thereby reducing the effective crater population available for statistical analysis. The apparent differences in uncertainties among the individual units are therefore most plausibly attributable to the limited surface area and the small number of preserved impact craters, which together diminish the statistical robustness of the CSFD fits.

Crater counting statistics can be influenced by several geological processes, including partial burial by lava flows, superposition of ejecta from larger impacts, obliteration of small craters by later impacts, and downslope mass wasting on steep terrain (Zhao et al., 2013). To minimize these effects, crater counts were restricted to relatively flat floor regions and excluded areas affected by steep slopes, obvious resurfacing, or dense secondary crater clusters. Secondary craters were systematically identified and removed during the counting process. As a result, the influence of secondary cratering and slope-related degradation on the derived age should be negligible.

Nevertheless, crater rays associated with the Taruntius crater superpose basaltic units in northwestern Mare Fecunditatis, indicating that the impact event postdates the emplacement of these basalts. Previous studies have dated the basalts in this region to 3.47–3.71 Ga (Hiesinger et al., 2006; Yue et al., 2025), with part of this age range younger than the absolute model age derived in this study. Two plausible explanations may account for this apparent discrepancy. First, earlier AMA age estimates for Mare Fecunditatis basalts were based on older and lower-resolution data sets (Hiesinger et al., 2006), potentially introducing systematic uncertainties into crater-based chronologies. Second, the limited surface area of the Taruntius crater floor and the relatively small number of countable craters may reduce the statistical robustness of the derived age estimates. Given the absence of typical, large-scale impact melt flow morphologies within the Taruntius crater, its formation age is like to be

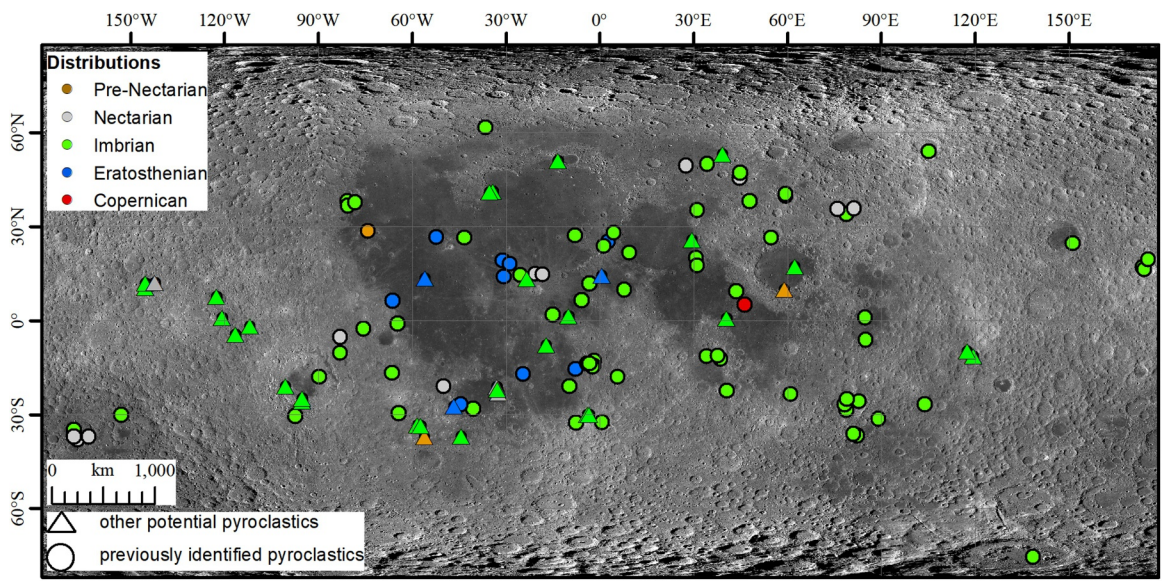


Figure 10. Spatial and temporal distribution of 75 lunar pyroclastic deposits (Gaddis et al., 2003; Gustafson et al., 2012). Identified pyroclastics deposits from Gaddis et al. (2003) and Gustafson et al. (2012) are marked by circles, whereas potential pyroclastics occurrences are marked by triangles, while colors indicating geological periods according to the lunar geological chronology map (Fortezzo et al., 2020). The projection is simple cylindrical projection.

relatively old. We therefore consider the 3.7 Ga model age of the floor unit to be robust, and infer that Taruntius formed during the Imbrian epoch.

5.2. Lifetime and Persistence of Crater Rays

Taruntius crater displays well-defined structural boundaries, a prominent central peak, and a complete radial ray system, whose morphological characteristics were traditionally associated with relatively young lunar impact craters. Consequently, early studies classified Taruntius as a Copernican-aged crater (Wilhelms & McCauley, 1971). Subsequent work, however, demonstrated that its bright rays are controlled primarily by compositional contrasts rather than optical immaturity, contributing to its reassignment to the Eratosthenian system (Hawke et al., 2004).

Our results confirm that the rays surrounding Taruntius are indeed of compositional origin and that their optical maturity is comparable to that of surrounding mare surfaces. Combined with the CSFD results and age constraints from the surrounding mare units, the floor of Taruntius crater is inferred to have formed during the Imbrian period. If volcanic activity partially resurfaced the crater floor after impact, which buried earlier craters and modified pre-existing structures, the CSFD-derived ages would represent minimum estimates. In such a scenario, the formation of the ejecta blanket, and hence the rays, must predate the resurfaced floor and therefore be substantially older than the Eratosthenian or Copernican periods.

The long-term preservation of compositional rays is not unique to Taruntius. A comparable example is Lichtenberg crater, which was initially classified as Copernican based on the presence of prominent rays (Shoemaker & Hackman, 1962) and subsequent mapping efforts (Wilhelms et al., 1987). However, the ejecta blanket of Lichtenberg exhibits OMAT values of ∼0.14–0.15, indistinguishable from those of mature surrounding mare surfaces, indicating that its ejecta materials are fully space-weathered. Geological relationships further constrain the age of Lichtenberg. Its ejecta are embayed by mare basalts dated to $1.68^{+0.30}_{-0.20}$ Ga, which themselves overlie older mare units dated to $3.18^{+0.08}_{-0.10}$ Ga (Hiesinger et al., 2003). These relationships require that the Lichtenberg impact occurred prior to ∼1.68 Ga and possibly significantly earlier.

Together, these observations demonstrate that the presence of crater rays is not a reliable criterion for identifying Copernican-aged impact craters. Instead, the preservation of compositional rays reflects the combined effects of space weathering, impact gardening, and mass wasting processes (Lucey et al., 2006). Complete removal of compositional rays requires both full optical maturation of the ejecta and sufficient impact-driven overturning to thoroughly mix ejecta material with the surrounding regolith, thereby reducing its spectral and compositional contrast over time (Hawke et al., 2004).

5.3. Constraining the Lifetime of Explosive Volcanism on the Moon

In addition to impact processes, volcanic activity has played a fundamental role in shaping the lunar surface and can significantly influence crater-based age determinations. For impact craters with fractured floors, two principal formation mechanisms have been proposed: viscous relaxation of the crust and magma intrusion(Jozwiak et al., 2012, 2015, 2017, 2018). The latter mechanism involves impact-induced fault and fracture networks beneath the crater floor (Johnson & Pollard, 1973), which act as conduits for ascending magma (Solomon & Head, 1980). As magma rises along dikes, increasing internal pressure can generate piston-like uplift of the crater floor, potentially followed by volcanic eruption.

During magma ascent, volatile components tend to exsolve and concentrate near the top of the dike. In the lunar near-vacuum environment, rapid pressure release can trigger explosive volcanic activity, producing regional pyroclastic deposits. With progressive volatile depletion, eruptive activity may transition to effusive lava emplacement, infilling the crater floor and surrounding areas. More than 100 pyroclastic deposits have been identified on the lunar surface (Gaddis et al., 2003; Gustafson et al., 2012). Based on their spatial distribution (Figure 10), our analysis confirms the presence of pyroclastic deposits within Taruntius crater (Figure 6), consistent with volcanic modification following crater formation. Therefore, the localized enrichment of olivine and pyroxenes south to the central peak is most likely associated with volcanic activity. In contrast, the central peak is interpreted to reflect the excavation and uplift of deep crustal materials during the formation of Taruntius crater. The region near the Cameron crater further suggests exposure of deeper crustal lithologies with mafic-enriched characteristics.

The timing of lunar volcanic activity is commonly constrained using CSFD dating and radiometric ages from lunar samples and meteorites (Hiesinger et al., 2011; Snape et al., 2018). Although the mechanisms and morphologies of lunar volcanism are well established, the cessation age of explosive volcanism remains debated (Qiao et al., 2020). Crater-based studies suggest that lunar volcanic activity was most intense between ∼4.0 and 1.2 Ga, with a pronounced peak between ∼4.0 and 3.5 Ga (Hiesinger et al., 2011). The CSFD-derived ages obtained for Taruntius crater fall within this principal interval of lunar volcanism, supporting the interpretation that volcanic resurfacing affected the crater floor.

Variations in model ages and associated uncertainties among individual floor units are likely influenced by post-impact magmatic activity. The degree to which lava flows modify crater populations depends primarily on lava thickness and crater size: sufficiently thick lava flows can bury small pre-existing craters, while larger craters remain partially preserved (Zhao et al., 2013). Floor1, floor2, and floor3 are close to the fracture zone, where lava flows likely partially or completely obscured smaller impact craters formed on the original crater floor. Such resurfacing can degrade crater rims and complicate diameter measurements, contributing to increased uncertainty in CSFD age estimates for volcanically modified areas.

Previous studies have shown that lava-covered surfaces commonly exhibit two-segment CSFD curves, with the older segment reflecting the formation age of the underlying unit and the younger segment recording resurfacing by lava flows (Zhao et al., 2013). In the case of Taruntius, the CSFD curves for the dated floor units do not display a clear two-population signature. This likely reflects the limited influence of lava flows on craters larger than the minimum diameter considered in this study (0.5 km). As smaller craters are more readily buried or erased by lava emplacement, the crater population used here is less sensitive to volcanic resurfacing. Consequently, despite local volcanic modification, the CSFD-derived ages for Taruntius crater are considered robust and representative of the primary formation age of the crater.

Prior to this work, the Taruntius crater was commonly interpreted as having formed during the Copernican or Eratosthenian periods (Gaddis et al., 2003; Jozwiak et al., 2015), and the pyroclastic deposits on its floor were regarded as the only recognized products of explosive volcanism potentially associated with a Copernican-aged geologic unit (Figure 10). This crater-based chronology, however, indicates that the model age of the volcanic activity zone on the Taruntius crater floor is substantially older. There is no evidence for explosive volcanic activity during the Copernican Period, thereby providing an important constraint on the timing of its cessation on the Moon.

6. Conclusions

Integrated geomorphological, spectral, and crater statistical analyses demonstrate that Taruntius crater records complex impact and volcanic modification of the lunar crust. Mineralogical mapping reveals systematic vertical compositional heterogeneity, with olivine- and low-calcium pyroxene–rich lithologies exposed in the central peak, contrasting with plagioclase-dominated materials in the crater walls and ejecta blanket. This distribution pattern reflects the geological process involving the excavation of the deeper lunar crust, combined with the emplacement of mafic magma and volcanic deposition.

Despite having reached optical maturity, the radial features surrounding Taruntius remain conspicuous in albedo, indicating that these rays are preserved by compositional contrasts rather than by optical immaturity. This observation provides direct evidence that ray visibility alone is insufficient for assigning Copernican ages to lunar impact craters.

Crater size-frequency distribution dating indicates that Taruntius formed significantly earlier than the Copernican period, most likely during the late Imbrian. This revised age, together with evidence for volcanic modification of the crater floor, experienced the influence of magmatic processes on crater morphology and crater-based chronology. More broadly, these results highlight the need to reevaluate ray-based stratigraphic criteria and provide new constraints on the temporal decay of impact flux.

Conflict of Interest

The authors declare no conflicts of interest relevant to this study.

Availability Statement

LROC WAC and NAC data are available from the LROC website (http://lroc.sese.asu.edu). Kaguya TC and MI data are available from SELENE Data Archive (https://darts.isas.jaxa.jp/app/pdap/selene/). The SLDEM2015 data and the GRAIL Bouguer gravity disturbance map are available at the Planetary Geodynamics Data Archive (https://pgda.gsfc.nasa.gov/products/). The LP GRS Th abundance map, rock abundance map, and M^3 data are available from PDS Geosciences Node (https://pds-geosciences.wustl.edu/default.htm). The GRAIL lunar crustal thickness model data were accessed from Zenodo repository (https://zenodo.org/records/997347). Kaguya Multiband Imager mineral maps are available from the United States Geological Survey at the Planetary Data System's Cartography and Imaging Sciences Node Annex (https://astrogeology.usgs.gov/search/map/lunar-kaguya-multiband-imager-mosaics). Crater Tools in ArcGIS is available from Kneissl et al. (2011) and CraterStats software is obtained from Michael and Neukum (2010).

Acknowledgments
This work was supported by the fundings from the National Natural Science Foundation (42402231, 42441817, 42241107, 42578002) and the National Key Research and Development Program of China (2022YFF0711400).

References

Bandfield, J. L., Ghent, R. R., Vasavada, A. R., Paige, D. A., Lawrence, S. J., & Robinson, M. S. (2011). Lunar surface rock abundance and regolith fines temperatures derived from LRO diviner radiometer data. *Journal of Geophysical Research*, *116*(E12), E00H02. https://doi.org/10.1029/2011JE003866

Barker, M. K., Mazarico, E., Neumann, G. A., Zuber, M. T., Haruyama, J., & Smith, D. E. (2016). A new lunar digital elevation model from the lunar orbiter laser altimeter and SELENE Terrain Camera. *Icarus*, *273*, 346–355. https://doi.org/10.1016/j.icarus.2015.07.039

Besse, S., Jawin, E., Mazrouei, S., Gaddis, L., & Sunshine, J. (2013). Spectral signature of lunar pyroclastic deposits in moon mineralogy (M3) data. In *Paper presented at the 44th Lunar and Planetary Science Conference*. Lunar and Planetary Institute. (abstract #1662).

Bussey, D. B. J., & Spudis, P. D. (2000). Compositional studies of the Orientale, Humorum, Nectaris, and Crisium lunar basins. *Journal of Geophysical Research*, *105*(E2), 4235–4243. https://doi.org/10.1029/1999JE001130

Byrne, P. K., Klimczak, C., McGovern, P. J., Mazarico, E., James, P. B., Neumann, G. A., et al. (2015). Deep-seated thrust faults bound the Mare Crisium lunar mascon. *Earth and Planetary Science Letters*, *427*, 183–190. https://doi.org/10.1016/j.epsl.2015.06.022

Carrier, W. D., III., Olhoeft, G. R., & Mendell, W. (1991). Physical properties of the lunar surface. In C. H. Heken, D. T. Vaniman & B. M. French (Eds), *Lunar Sourcebook, A User's Guide to the Moon* (Vol. 475, pp. 475–594).

Eberhardt, P., Geiss, J., Grögler, N., & Stettler, A. (1973). How old is the crater Copernicus? *The Moon*, *8*(1), 104–114. https://doi.org/10.1007/BF00562752

Elder, C. M., Hayne, P. O., Bandfield, J. L., Ghent, R. R., Williams, J. P., Donaldson Hanna, K. L., & Paige, D. A. (2017). Young lunar volcanic features: Thermophysical properties and formation. *Icarus*, *290*, 224–237. https://doi.org/10.1016/j.icarus.2017.03.004

Fortezzo, C. M., Spudis, P. D., & Harrel, S. L. (2020). Release of the digital unified global geologic map of the moon at 1:5,000,000-Scale. In *Paper presented at the 51st Lunar and Planetary Science Conference*. Lunar and Planetary Institute.

Gaddis, L. R., Staid, M. I., Tyburczy, J. A., Hawke, B. R., & Petro, N. E. (2003). Compositional analyses of lunar pyroclastic deposits. *Icarus*, *161*(2), 262–280. https://doi.org/10.1016/S0019-1035(02)00036-2

Ghent, R. R., Hayne, P. O., Bandfield, J. L., Campbell, B. A., Allen, C. C., Carter, L. M., & Paige, D. A. (2014). Constraints on the recent rate of lunar ejecta breakdown and implications for crater ages. *Geology*, *42*(12), 1059–1062. https://doi.org/10.1130/G35926.1

Goossens, S., Sabaka, T. J., Wieczorek, M. A., Neumann, G. A., Mazarico, E., Lemoine, F. G., et al. (2020). High-resolution gravity field models from GRAIL data and implications for models of the density structure of the moon's crust. *Journal of Geophysical Research: Planets*, *125*(2), e2019JE006086. https://doi.org/10.1029/2019JE006086

Gustafson, J., Bell, J. F., Gaddis, L., Hawke, B., & Giguere, T. (2012). Characterization of previously unidentified lunar pyroclastic deposits using lunar reconnaissance orbiter camera (LROC) data. *Journal of Geophysical Research*, *117*(E12). https://doi.org/10.1029/2011JE003893

Hartung, J. B., Hodges, F., Horz, F., & Storzer, D. (1975). Microcrater investigations of lunar rock 12002. *Proceedings of the Lunar and Planetary Science Conference*, *3*, 3351–3371.

Haruyama, J., Matsunaga, T., Ohtake, M., Morota, T., Honda, C., Yokota, Y., et al. (2008). Global lunar-surface mapping experiment using the lunar Imager/spectrometer on SELENE. *Earth, Planets and Space*, *60*(4), 243–255. https://doi.org/10.1186/BF03352788

Hawke, B. R., Blewett, D. T., Lucey, P. G., Smith, G. A., Bell, J. F., Campbell, B. A., & Robinson, M. S. (2004). The origin of lunar crater rays. *Icarus*, *170*(1), 1–16. https://doi.org/10.1016/j.icarus.2004.02.013

Head, J. W., III., & Wilson, L. (1979). Alphonsus-type dark-halo craters: Morphology, morphometry and eruption conditions. *Proceedings of the Lunar and Planetary Science Conference*, *3*, 2861–2897.

Hiesinger, H., Head, I. J. W., Wolf, U., Jaumann, R., & Neukum, G. (2003). Ages and stratigraphy of mare basalts in Oceanus Procellarum, Mare Nubium, Mare Cognitum, and Mare Insularum. *Journal of Geophysical Research*, *108*(E7). https://doi.org/10.1029/2002JE001985

Hiesinger, H., Head, J. W., III., Wolf, U., Jaumann, R., & Neukum, G. (2006). New ages for basalts in mare fecunditatis based on crater size-frequency measurements. In *Paper presented at 37th Lunar and Planetary Science Conference*.Lunar and Planetary Institute. (abstract #1151).

Hiesinger, H., Head, J. W., Wolf, U., Jaumann, R., & Neukum, G. (2011). Ages and stratigraphy of lunar mare basalts: A synthesis. *Special Paper of the Geological Society of America*, *477*, 1–51. https://doi.org/10.1130/2011.2477(01)

Hiesinger, H., Jaumann, R., Neukum, G., & Head Iii, J. W. (2000). Ages of mare basalts on the lunar nearside. *Journal of Geophysical Research*, *105*(E12), 29239–29275. https://doi.org/10.1029/2000JE001244

Hiesinger, H., van der Bogert, C. H., Pasckert, J. H., Funcke, L., Giacomini, L., Ostrach, L. R., & Robinson, M. S. (2012). How old are young lunar craters? *Journal of Geophysical Research*, *117*(E12). https://doi.org/10.1029/2011JE003935

Hou, X., Cao, H., Fu, X., Zhang, J., Li, B., & Ling, Z. (2022). Formation and degradation of lunar crater ray and possible geochronology application. *Chinese Journal of Space Science*, *42*(1), 127. https://doi.org/10.11728/cjss2022.01.201014091

Johnson, A. M., & Pollard, D. D. (1973). Mechanics of growth of some laccolithic intrusions in the Henry mountains, Utah, I: Field observations, Gilbert's model, physical properties and flow of the magma. *Tectonophysics*, *18*(3), 261–309. https://doi.org/10.1016/0040-1951(73)90050-4

Jozwiak, L. M., Head, J. W., & Wilson, L. (2015). Lunar floor-fractured craters as magmatic intrusions: Geometry, modes of emplacement, associated tectonic and volcanic features, and implications for gravity anomalies. *Icarus*, *248*, 424–447. https://doi.org/10.1016/j.icarus.2014.10.052

Jozwiak, L. M., Head, J. W., & Wilson, L. (2018). Explosive volcanism on Mercury: Analysis of vent and deposit morphology and modes of eruption. *Icarus*, *302*, 191–212. https://doi.org/10.1016/j.icarus.2017.11.011

Jozwiak, L. M., Head, J. W., Zuber, M. T., Smith, D. E., & Neumann, G. A. (2012). Lunar floor-fractured craters: Classification, distribution, origin and implications for magmatism and shallow crustal structure. *Journal of Geophysical Research*, *117*(E11). https://doi.org/10.1029/2012JE004134

Jozwiak, L. M., Head, J. W., III., Neumann, G. A., & Wilson, L. (2017). Observational constraints on the identification of shallow lunar magmatism: Insights from floor-fractured craters. *Icarus*, *283*, 224–231. https://doi.org/10.1016/j.icarus.2016.04.020

Kneissl, T., van Gasselt, S., & Neukum, G. (2011). Map-projection-independent crater size-frequency determination in GIS environments—New software tool for ArcGIS. *Planetary and Space Science*, *59*(11), 1243–1254. https://doi.org/10.1016/j.pss.2010.03.015

Lawrence, D. J., Feldman, W. C., Elphic, R. C., Little, R. C., Prettyman, T. H., Maurice, S., et al. (2002). Iron abundances on the lunar surface as measured by the lunar prospector gamma-ray and neutron spectrometers. *Journal of Geophysical Research*, *107*(E12), 13-11–26. https://doi.org/10.1029/2001JE001530

Lemelin, M., Lucey, P., Song, e., & Taylor, J. (2015). Lunar central peak mineralogy and iron content using the Kaguya multiband imager: Reassessment of the compositional structure of the lunar crust. *Journal of Geophysical Research: Planets*, *120*(5), 869–887. https://doi.org/10.1002/2014JE004778

Lemelin, M., Lucey, P. G., Miljković, K., Gaddis, L. R., Hare, T., & Ohtake, M. (2019). The compositions of the lunar crust and upper mantle: Spectral analysis of the inner rings of lunar impact basins. *Planetary and Space Science*, *165*, 230–243. https://doi.org/10.1016/j.pss.2018.10.003

Lev, E., Hamilton, C. W., Voigt, J. R. C., Stadermann, A. C., Zhan, Y., & Neish, C. D. (2021). Emplacement conditions of lunar impact melt flows. *Icarus*, *369*, 114578. https://doi.org/10.1016/j.icarus.2021.114578

Li, C., Liu, J., Ren, X., Mou, L., Zou, Y., Zhang, H., et al. (2010). The global image of the moon obtained by the Chang'E-1: Data processing and lunar cartography. *Science China Earth Sciences*, *53*(8), 1091–1102. https://doi.org/10.1007/s11430-010-4016-x

Lu, X., Cao, H., Ling, Z., Fu, X., Qiao, L., & Chen, J. (2021). Geomorphology, mineralogy, and geochronology of mare basalts and non-mare materials around the lunar Crisium basin. *Remote Sensing*, *13*(23), 4828. https://doi.org/10.3390/rs13234828

Lucey, P., Korotev, R. L., Gillis, J. J., Taylor, L. A., Lawrence, D., Campbell, B. A., et al. (2006). Understanding the lunar surface and space-moon interactions. In B. L. Jolliff & M. A. Wieczorek (Eds.), *New views of the moon*. (Vol. 16(1), pp. 83–219). https://doi.org/10.2138/rmg.2006.60.2

Lucey, P. G., Blewett, D. T., Taylor, G. J., & Hawke, B. R. (2000). Imaging of lunar surface maturity. *Journal of Geophysical Research*, *105*(E8), 20377–20386. https://doi.org/10.1029/1999je001110

Melosh, H. J. (1979). Acoustic fluidization: A new geologic process? *Journal of Geophysical Research*, *84*(B13), 7513–7520. https://doi.org/10.1029/JB084iB13p07513

Melosh, H. J. (1989). Impact cratering: A geologic process. *The Journal of Geology*, *97*(6), 773–773. https://doi.org/10.1086/629363

Mendell, W. W. (1976). Degradation of large, period II lunar craters. *Proceedings of the Lunar and Planetary Science Conference*, *3*, 2705–2716.

Meyer, C., Jr., Brett, R., Hubbard, N. J., Morrison, D. A., McKay, D. S., Aitken, F. K., et al. (1971). Mineralogy, chemistry, and origin of the KREEP component in soil samples from the ocean of storms. *Proceedings of the Lunar and Planetary Science Conference*, *2*, 393.

Michael, G. G., & Neukum, G. (2010). Planetary surface dating from crater size–frequency distribution measurements: Partial resurfacing events and statistical age uncertainty. *Earth and Planetary Science Letters*, *294*(3), 223–229. https://doi.org/10.1016/j.epsl.2009.12.041

Michael, G. G., Platz, T., Kneissl, T., & Schmedemann, N. (2012). Planetary surface dating from crater size–frequency distribution measurements: Spatial randomness and clustering. *Icarus*, *218*(1), 169–177. https://doi.org/10.1016/j.icarus.2011.11.033

Mustard, J. F., Pieters, C. M., Isaacson, P. J., Head, J. W., Besse, S., Clark, R. N., et al. (2011). Compositional diversity and geologic insights of the Aristarchus crater from moon mineralogy mapper data. *Journal of Geophysical Research*, *116*(E6), E00G12. https://doi.org/10.1029/2010JE003726

Neukum, G., Ivanov, B. A., & Hartmann, W. K. (2001). Cratering records in the inner solar system in relation to the lunar reference system. *Space Science Reviews*, *96*(1), 55–86. https://doi.org/10.1023/A:1011989004263

Neumann, G., Zuber, M., Wieczorek, M., Head, J., Baker, D., Solomon, S., et al. (2015). Lunar impact basins revealed by gravity recovery and interior laboratory measurements. *Science Advances*, *1*(9), e1500852. https://doi.org/10.1126/sciadv.1500852

Otake, H., Ohtake, M., & Hirata, N. (2012). Lunar iron and titanium abundance algorithms based on SELENE (Kaguya) multiband imager data. In *Paper presented at the In: 43rd Lunar and Planetary Science Conference*. Lunar and Planetary Institute. *(abstract #1905)*.

Pieters, C. M., Adams, J. B., Mouginis-Mark, P. J., Zisk, S. H., Smith, M. O., Head, J. W., & McCord, T. B. (1985). The nature of crater rays: The Copernicus example. *Journal of Geophysical Research*, *90*(B14), 12393–12413. https://doi.org/10.1029/JB090iB14p12393

Pieters, C. M., Boardman, J., Buratti, B., Chatterjee, A., Clark, R., Glavich, T., et al. (2009). The moon mineralogy mapper (M3) on Chandrayaan-1. *Current Science*, *96*(4), 500–505.

Pieters, C. M., Staid, M. I., Fischer, E. M., Tompkins, S., & He, G. (1994). A sharper view of impact craters from clementine data. *Science*, *266*(5192), 1844–1848. https://doi.org/10.1126/science.266.5192.1844

Qiao, L., Head, J. W., Ling, Z., & Wilson, L. (2020). Lunar irregular mare patches: Classification, characteristics, geologic settings, updated catalog, origin, and outstanding questions. *Journal of Geophysical Research: Planets*, *125*(7), e2019JE006362. https://doi.org/10.1029/2019JE006362

Qiao, L., Head, J. W., Wilson, L., Chen, J., & Ling, Z. (2021). Mare domes in mare tranquillitatis: Identification, characterization, and implications for their origin. *Journal of Geophysical Research: Planets*, *126*(9), e2021JE006888. https://doi.org/10.1029/2021JE006888

Robinson, M. S., Brylow, S. M., Tschimmel, M., Humm, D., Lawrence, S. J., Thomas, P. C., et al. (2010). Lunar reconnaissance orbiter camera (LROC) instrument overview. *Space Science Reviews*, *150*(1), 81–124. https://doi.org/10.1007/s11214-010-9634-2

Runyon, K. D., Moriarty, D. P., III., Denevi, B. W., Greenhagen, B. T., Morgan, G., Young, K. E., et al. (2020). Impact melt facies in the moon's Crisium basin: Identifying, characterizing, and future radiogenic dating. *Journal of Geophysical Research: Planets*, *125*(1), e2019JE006024. https://doi.org/10.1029/2019JE006024

Schultz, P. H. (1976). Floor-fractured lunar craters. *The Moon*, *15*(3), 241–273. https://doi.org/10.1007/BF00562240

Schultz, P. H. (1996). Nature of the Orientale and Crisium impacts. In *Paper presented at the 27th Lunar and Planetary Science Conference*. Lunar and Planetary Institute. (abstract #1147).

Schultz, P. H., & Spudis, P. D. (1983). Beginning and end of lunar mare volcanism. *Nature*, *302*(5905), 233–236. https://doi.org/10.1038/302233a0

Shkuratov, Y. G., & Bondarenko, N. V. (2001). Regolith layer thickness mapping of the moon by radar and optical data. *Icarus*, *149*(2), 329–338. https://doi.org/10.1006/icar.2000.6545

Shoemaker, E., Batson, R., Holt, H., Morris, E., Rennilson, J., & Whitaker, E. (1968). Television observations from Surveyor 3. *Journal of Geophysical Research*, *73*(12), 3989–4043. https://doi.org/10.1029/JB073i012p03989

Shoemaker, E. M., Batson, R. M., Holt, H. E., Morris, E. C., Rennilson, J. J., & Whitaker, E. A. (1969). Observations of the lunar regolith and the Earth from the television camera on Surveyor 7. *Journal of Geophysical Research*, *74*(25), 6081–6119. https://doi.org/10.1029/JB074i025p06081

Shoemaker, E. M., & Hackman, R. J. (1962). Stratigraphic basis for a lunar time scale. In Z. Kopal & Z. K. Mikhailov (Eds.), The Moon—Symposium 14 of the International Astronomical Union (pp. 289–300). Academic Press.

Singer, K. N., Jolliff, B. L., & McKinnon, W. B. (2020). Lunar secondary craters and estimated ejecta block sizes reveal a scale-dependent fragmentation trend. *Journal of Geophysical Research: Planets*, *125*(8), e2019JE006313. https://doi.org/10.1029/2019JE006313

Snape, J., Curran, N., Whitehouse, M., Nemchin, A., Joy, K., Hopkinson, T., et al. (2018). Ancient volcanism on the moon: Insights from Pb isotopes in the MIL 13317 and Kalahari 009 lunar meteorites. *Earth and Planetary Science Letters*, *502*, 84–95. https://doi.org/10.1016/j.epsl.2018.08.035

Solomon, S. C., & Head, J. W. (1980). Lunar mascon basins: Lava filling, tectonics, and evolution of the lithosphere. *Reviews of Geophysics*, *18*(1), 107–141. https://doi.org/10.1029/RG018i001p00107

Spudis, P. D., & Sliz, M. U. (2017). Impact melt of the lunar Crisium multiring basin. *Geophysical Research Letters*, *44*(3), 1260–1265. https://doi.org/10.1002/2016GL071429

Thapa, J., Sur, K., Chauhan, M., Ghosh, B., Kundu, A., Pundir, E., et al. (2025). Deciphering mineralogical and compositional variations in lunar basin, mare fecunditatis: An in-depth analysis using hyperspectral remote sensing techniques. *Advances in Space Research*, *75*(4), 4080–4098. https://doi.org/10.1016/j.asr.2024.12.023

Vasavada, A. R., Bandfield, J. L., Greenhagen, B. T., Hayne, P. O., Siegler, M. A., Williams, J.-P., & Paige, D. A. (2012). Lunar equatorial surface temperatures and regolith properties from the diviner lunar radiometer experiment. *Journal of Geophysical Research*, *117*(E12), E00H18. https://doi.org/10.1029/2011JE003987

Wentworth, S. J., McKay, D. S., Lindstrom, D. J., Basu, A., Martinez, R. R., Bogard, D. D., & Garrison, D. H. (1994). Apollo 12 ropy glasses revisited. *Meteoritics*, *29*(3), 323–333. https://doi.org/10.1111/j.1945-5100.1994.tb00596.x

Wichman, R. W., & Schultz, P. H. (1996). Crater-centered laccoliths on the moon: Modeling intrusion depth and magmatic pressure at the crater Taruntius. *Icarus*, *122*(1), 193–199. https://doi.org/10.1006/icar.1996.0118

Wieczorek, M. A., Neumann, G. A., Nimmo, F., Kiefer, W. S., Taylor, G. J., Melosh, H. J., et al. (2013). The crust of the moon as seen by GRAIL. *Science*, *339*(6120), 671–675. https://doi.org/10.1126/science.1231530

Wilhelms, D., McCauley, J. F., & Trask, N. (1987). *The geologic history of the Moon*. U.S. Geological Survey Report. https://doi.org/10.3133/pp1348

Wilhelms, D. E., & McCauley, J. F. (1971). *Geologic map of the near side of the Moon*. U.S. Geological Survey Report. https://doi.org/10.3133/i703

Xie, M., Xiao, Z., & Xu, A. (2019). Time-dependent production functions of lunar simple craters on layered targets with consideration of topographic degradation. *Geophysical Research Letters*, *46*(20), 10987–10996. https://doi.org/10.1029/2019GL084097

Yu, H., Wang, G., Xu, C., Chai, Y., Bie, L., & Cui, L. (2024). Insight into three-dimensional structure of the lunar crust and upper mantle in the Mare Crisium from gravity imaging. *Advances in Space Research*, *74*(3), 1378–1391. https://doi.org/10.1016/j.asr.2024.04.061

Yue, Z., Sun, S., Du, J., Gou, S., Di, K., Wang, Y., et al. (2025). New insights into the geological evolution history of mare fecunditatis. *Icarus*, *425*, 116348. https://doi.org/10.1016/j.icarus.2024.116348

Zanetti, M., Stadermann, A., Jolliff, B., Hiesinger, H., van der Bogert, C. H., & Plescia, J. (2017). Evidence for self-secondary cratering of Copernican-age continuous ejecta deposits on the moon. *Icarus*, *298*, 64–77. https://doi.org/10.1016/j.icarus.2017.01.030

Zhang, L., Zhang, X., Yang, M., Xiao, X., Qiu, D., Yan, J., et al. (2023). New maps of major oxides and Mg # of the lunar surface from additional geochemical data of Chang'E-5 samples and KAGUYA multiband imager data. *Icarus*, *397*, 115505. https://doi.org/10.1016/j.icarus.2023.115505

Zhao, J., Huang, J., Xiao, L., Qiao, L., Wang, J., & Hu, S. Y. (2013). Crater size-frequency distribution measurements and age determination of Sinus Iridum. *Earth Science*, *38*, 351–361. https://doi.org/10.3799/dqkx.2013.034

Zhao, J., Qiao, L., Zhang, F., Yuan, Y., Huang, Q., Yan, J., et al. (2023). Volcanism and deep structures of the moon. *Space: Science and Technology*, *3*, 0076. https://doi.org/10.34133/space.0076

Zhao, S., Qian, Y., Xiao, L., Zhao, J., He, Q., Huang, J., et al. (2022). Lunar mare fecunditatis: A science-rich region and a concept mission for long-distance exploration. *Remote Sensing*, *14*(5), 1062. https://doi.org/10.3390/rs14051062